

Squeeze free space with nonlocal flat optics

CHENG GUO,¹  HAIWEN WANG,¹ AND SHANHUI FAN^{2,*}

¹Department of Applied Physics, Stanford University, Stanford, California 94305, USA

²Ginzton Laboratory and Department of Electrical Engineering, Stanford University, Stanford, California 94305, USA

*Corresponding author: shanhui@stanford.edu

Received 16 March 2020; revised 12 July 2020; accepted 25 July 2020 (Doc. ID 392978); published 3 September 2020

There has been substantial interest in miniaturizing optical systems by flat optics. However, one essential optical component, free space, fundamentally cannot be substituted with conventional local flat optics with space-dependent transfer functions, since the transfer function of free space is momentum-dependent instead. Overcoming this difficulty is important to achieve the utmost miniaturization of optical systems. In this work, we show that free space can be substituted with nonlocal flat optics operating directly in the momentum domain. We derive the general criteria for an optical device to replace free space and provide two concrete designs of photonic crystal slab devices. Such devices can substitute much thicker free space. Our work paves the way for the utmost miniaturization of optical systems using a combination of local and nonlocal flat optics. © 2020 Optical Society of America under the terms of the [OSA Open Access Publishing Agreement](#)

<https://doi.org/10.1364/OPTICA.392978>

1. INTRODUCTION

Recently, there has been significant progress in flat optics aiming to miniaturize optical systems by replacing conventional optical components [1–4]. Such flat optics typically achieve wavefront shaping through local control of phase, amplitude, and polarization in the spatial domain. This approach enables compact devices including metalenses, beam deflectors, and holograms, with potential applications such as flat displays, wearable optics, and lightweight imaging systems [5].

However, there is one essential optical component that has been long overlooked in flat optics: free space. Free space is an essential part of most optical systems and usually constitutes a great portion of the system volume. The utmost miniaturization of optical systems therefore requires significant reduction of free space: a truly miniaturized imaging system needs not only compact flat lenses, but also squeezed free space.

Free space fundamentally cannot be substituted with conventional local flat optics characterized by space-dependent transfer functions, since the free space propagation has a momentum-dependent transfer function instead. On the other hand, recently there has been significant interest in lensless Fourier optics using nonlocal photonic nanostructures with transfer functions in the momentum domain. This approach enables important functionalities in optical analog processing including optical differentiation, filtering, and phase mining using compact devices [6–16].

In this work, we show that free space can be substituted with nonlocal flat optics. We derive the general criteria for a device to replace free space and provide two concrete designs of such a device utilizing photonic Fano resonances. The device can substitute much thicker free space with a compression ratio as high as 144.

The device can be designed to adapt to different numerical apertures (NAs). It can be placed anywhere in the optical path to reduce free space as needed. Our work therefore opens up significant opportunities in miniaturizing optical systems by squeezing free space with nonlocal flat optics.

The rest of this paper is organized as follows. In Section 2, we provide a theoretical analysis of replacing free space with flat optics using Fano resonances. In Section 3, we provide numerical demonstration of two concrete photonic crystal slab designs to realize such functionality. We conclude in Section 4.

2. THEORETICAL ANALYSIS

In this section, we provide a theoretical analysis on substituting free space with flat optics.

First, we briefly examine the propagation of light in free space. Consider a monochromatic optical wave of wavelength λ and complex amplitude $U(x, y, z)$ in the free space between the input plane $z = 0$ and the output plane $z = d$. The free space propagation that maps $U(x, y, 0)$ to $U(x, y, d)$ is a shift-invariant linear system, since the Helmholtz equation that governs $U(x, y, z)$ is linear, and free space is invariant under spatial translation in the xy plane. Such a shift-invariant linear system is characterized by its transfer function [17]:

$$H(k_x, k_y) = \exp\left(-id\sqrt{k_0^2 - k_x^2 - k_y^2}\right), \quad (1)$$

where $\mathbf{k} = (k_x, k_y)$ is the in-plane wavevector, and $k_0 = 2\pi/\lambda$ is the angular wavenumber in free space. $H(k_x, k_y)$ is a circularly symmetric complex function of k_x and k_y . A plane wave component with $k_x^2 + k_y^2 \leq k_0^2$ is propagating. For such a wave,

the magnitude $|H(k_x, k_y)| = 1$, and the phase $\arg\{H(k_x, k_y)\}$ is wavevector dependent. A plane wave component with $k_x^2 + k_y^2 > k_0^2$ is evanescent. For such a wave, $H(k_x, k_y)$ is exponentially decaying.

Given the input field $U(x, y, 0)$, the output field $U(x, y, d)$ is determined as

$$U(x, y, d) = \iint_{-\infty}^{\infty} H(k_x, k_y) \tilde{U}(k_x, k_y, 0) \exp[-i(k_x x + k_y y)] dk_x dk_y, \quad (2)$$

where

$$\tilde{U}(k_x, k_y, 0) = \frac{1}{(2\pi)^2} \iint_{-\infty}^{\infty} U(x, y, 0) \exp[i(k_x x + k_y y)] dx dy. \quad (3)$$

In many cases of interest, the optical waves are paraxial where the input field $U(x, y, 0)$ contains only wavevector components for which $k_x^2 + k_y^2 \ll k_0^2$. The transfer function in Eq. (1) then can be simplified as

$$H(k_x, k_y) \approx H_0 \exp\left[i \frac{\lambda d}{4\pi} (k_x^2 + k_y^2)\right], \quad (4)$$

where $H_0 = \exp(-ik_0 d)$ is a global phase. This is the well-known Fresnel approximation [18]. This approximation is applicable if

$$\frac{(k_x^2 + k_y^2) \lambda^3 d}{64\pi^4} \ll 1. \quad (5)$$

In order to squeeze free space of a propagation distance d , our objective will be to create an optical device with the same transfer function of Eq. (4), but with a physical thickness that is much lesser than d . Since the transfer function of Eq. (4) describes a wavevector-dependent phase shift, with no mixing between different wavevector components, the required optical device must be periodic in order to preserve the wavevector as light transmits through the device. This is in contrast with standard metasurfaces, which are characterized by a space-dependent phase shift, and hence do not preserve the wavevector in the transmission process [11,19]. In addition, to achieve Eq. (4), ideally we will need an all-pass filter with unity amplitude transmission coefficient for all wavevector components.

In this work, we show that the transfer function of Eq. (4) can be achieved utilizing the phase response of Fano resonances [20–22]. We consider a single band of guided resonances in a two-dimensional (2D) photonic crystal slab. Assuming that the slab has mirror symmetry in the vertical direction (z direction), the transmitted and reflected amplitudes' near-resonant frequencies can be expressed as [23]

$$t(\omega, \mathbf{k}) = t_d + f \frac{\gamma(\mathbf{k})}{i(\omega - \omega(\mathbf{k})) + \gamma(\mathbf{k})}, \quad (6)$$

$$r(\omega, \mathbf{k}) = r_d \pm f \frac{\gamma(\mathbf{k})}{i(\omega - \omega(\mathbf{k})) + \gamma(\mathbf{k})}, \quad (7)$$

where t_d and r_d are the direct transmission and reflection coefficients, $\omega(\mathbf{k})$ and $\gamma(\mathbf{k})$ are the center frequencies and radiative linewidths of the guided resonance band, and f is the normalized complex amplitude. The plus/minus sign in Eq. (7) corresponds to even/odd mode with respect to the z -mirror plane, respectively.

For such a system, energy conservation requires [23,24]

$$f = -(t_d \pm r_d), \quad (8)$$

$$|r_d|^2 + |t_d|^2 = 1, \quad (9)$$

$$r_d/t_d \equiv -iq, \quad q \in \mathbb{R}. \quad (10)$$

Denote dimensionless frequency detuning as

$$\Omega(\omega, \mathbf{k}) = \frac{\omega - \omega(\mathbf{k})}{\gamma(\mathbf{k})}, \quad (11)$$

then Eq. (6) with Eqs. (8)–(10) becomes

$$t(\Omega) = t_d \frac{i(\Omega \pm q)}{1 + i\Omega}, \quad (12)$$

which is a typical Fano lineshape function, with $\pm q$ being the asymmetric parameter [25], and $|t_d| = 1/\sqrt{1+q^2}$. Near the resonance, the transmission magnitude varies between $|t| = 0$ at $\Omega = \mp q$ and $|t| = 1$ at $\Omega = \pm 1/q$. The phase also exhibits a rapid variation as a function of frequency:

$$\arg[t(\Omega)] = \arg(t_d) + \frac{\pi}{2} \text{sgn}(\Omega \pm q) - \arctan(\Omega), \quad (13)$$

where the first term corresponds to the phase of the directly transmitted amplitude, which is slowly varying in ω and \mathbf{k} ; the second term describes the abrupt π phase jump at the zero transmission frequency; the last term corresponds to the rapid variation of the phase due to the guided resonance.

Now, we show that the band dispersion of guided resonances can be used to realize the quadratic phase response as described by Eq. (4). We consider a specific band of guided resonances near $\mathbf{k} = \mathbf{0}$ with isotropic band dispersion,

$$\omega(\mathbf{k}) \approx \omega_0 + \alpha(k_x^2 + k_y^2), \quad (14)$$

where α describes the curvature of the band dispersion, and near-zero dispersion of linewidths

$$\gamma(\mathbf{k}) \approx \gamma_0. \quad (15)$$

Then, Eq. (11) becomes

$$\Omega(\omega, \mathbf{k}) \approx \Omega_0 - \frac{\alpha}{\gamma_0} (k_x^2 + k_y^2), \quad (16)$$

where

$$\Omega_0 \equiv \Omega(\omega, \mathbf{0}) = \frac{\omega - \omega_0}{\gamma_0}. \quad (17)$$

Assuming $\Omega(\omega, \mathbf{k}) \neq \mp q$ for all relevant \mathbf{k} , we substitute Eq. (16) into Eq. (13) and perform a Taylor series expansion to obtain

$$\arg[t(\Omega)] \approx \arg[t(\Omega_0)] + \frac{\alpha}{\gamma_0(1 + \Omega_0^2)} (k_x^2 + k_y^2), \quad (18)$$

which gives the same quadratic dependent of phase on the wavevector, as required in Eq. (4).

Finally, we note that by choosing suitable q and operating frequency $\omega \approx \pm 1/q$ correspondingly, in general, one can achieve near-unity transmission $|t(\Omega(\omega, \mathbf{k}))| \approx 1$ for all the relevant \mathbf{k} . Therefore, the transfer function for monochromatic waves with frequency ω becomes

$$t(k_x, k_y) = t(\Omega_0) \exp\left[i \frac{\alpha}{\gamma_0(1 + \Omega_0^2)} (k_x^2 + k_y^2)\right], \quad (19)$$

where $t(\Omega_0)$ is a global phase with $|t(\Omega_0)| = 1$. Equation (19) has exactly the same form as Eq. (4). Thus, we have shown that the same phase response for light propagating over a distance d_{eff} in free space can instead be achieved using a photonic crystal slab, provided that the band structure of the slab is isotropic as described by Eq. (14) with the parameters that satisfy

$$d_{\text{eff}} = \frac{4\pi\alpha}{\lambda\gamma_0(1 + \Omega_0^2)}. \quad (20)$$

With a choice of small γ_0 , (i.e., using guided resonances with high-quality factors), one can achieve a large d_{eff} using a photonic crystal slab with a physical thickness that is far smaller than d_{eff} . Therefore, we have shown that the use of a properly designed photonic crystal slab can achieve the squeezing of free space.

As was noted in Ref. [10], in a typical photonic crystal slab, due to the photonic spin-orbit coupling, the band structure near $\mathbf{k} = \mathbf{0}$ is not isotropic. However, one can use the specific design procedure as discussed in Ref. [10] to design a photonic crystal slab with an isotropic band structure of the form of Eq. (14). In the next section, we will follow the similar design procedure of Ref. [10] in our numerical design.

3. NUMERICAL DEMONSTRATION

Based on the theoretical considerations above, we provide two concrete designs of such a photonic crystal slab device. Our first device consists of three layers, as shown in Fig. 1(c). The middle layer is a photonic crystal slab with a lattice constant a . It has a thickness of $d = 0.55a$ and contains a square array of circular holes with radius $r = 0.111a$. Two homogeneous slabs with thickness $d_s = 0.07a$ are placed symmetrically besides the photonic crystal slab. The air gaps between the middle slab and the homogeneous slabs are $d_g = 0.94a$. We choose suitable d and r to achieve the isotropic band structure and d_g and d_s to realize the required background transmission t_d . The total thickness of such a device is $d_T = d + 2d_s + 2d_g = 2.57a$. All slabs are made of materials with a permittivity $\varepsilon = 12$, which approximates that of Si or GaAs in the infrared wavelength range.

Such a photonic crystal slab device hosts a pair of guided resonances that are doubly degenerate at the Γ point ($\mathbf{k} = \mathbf{0}$) with the

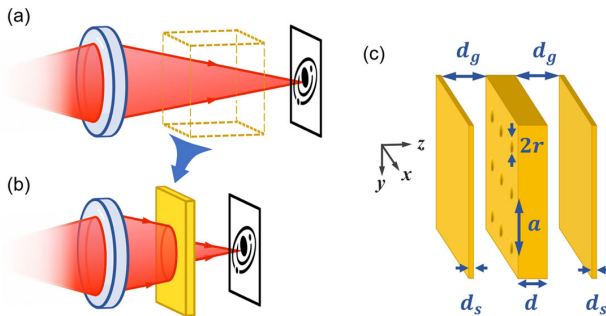


Fig. 1. (a) General optical system, showing the lens (blue), light beam (red), and a formed image. The free space propagation is highlighted as the dashed box. (b) The free space propagation can be replaced by a nonlocal optical device, which has a significantly reduced physical length, but performs the same functionality as the free space. (c) Properly designed photonic crystal slab can serve as a substitute for free space propagation. It contains a square lattice of air holes. The geometric parameters are $r = 0.111a$, $d = 0.55a$, $d_s = 0.07a$, and $d_g = 0.94a$. a is the periodicity along both the x and y directions. The yellow regions correspond to material with permittivity $\varepsilon = 12$.

frequency $\omega_0 = 0.47656 \times 2\pi c/a$. (Such a two-fold degeneracy is required in order for the guided resonance to couple to normally incident light [23].) As we mentioned above, in general, the band structure of the guided resonances is anisotropic around $\mathbf{k} = \mathbf{0}$ for a photonic crystal slab with the C_{4v} symmetry. However, with the geometry parameters chosen above, which are obtained following the same procedure as in Ref. [10], we show the corresponding band structure as obtained using the guided mode expansion method [26,27] in Fig. 2. Figure 2(a) shows that for each band the dispersion along the ΓX coincides with that along the ΓM direction. Figure 2(b) shows that the isofrequency contours for the upper band are almost circular. Both bands become almost completely isotropic:

$$\omega_i(\mathbf{k}) \approx \omega_0 + \alpha_i(k_x^2 + k_y^2), \quad i = 1, 2, \quad (21)$$

where $\alpha_1 = 1.79ca/(2\pi)$, $\alpha_2 = -0.43ca/(2\pi)$, and the 1,2 subscripts correspond to the upper and lower band, respectively [cf. Eq. (14)]. Also, we note that the dispersion of radiative linewidths $\gamma_i(\mathbf{k})$ is anisotropic. Nonetheless, the dispersion of $\gamma_i(\mathbf{k})$ is much smaller than that of $\omega_i(\mathbf{k})$ so that its effect on transfer function is negligible: $\gamma_i(\mathbf{k}) \approx \gamma_0$ [cf. Eq. (15)].

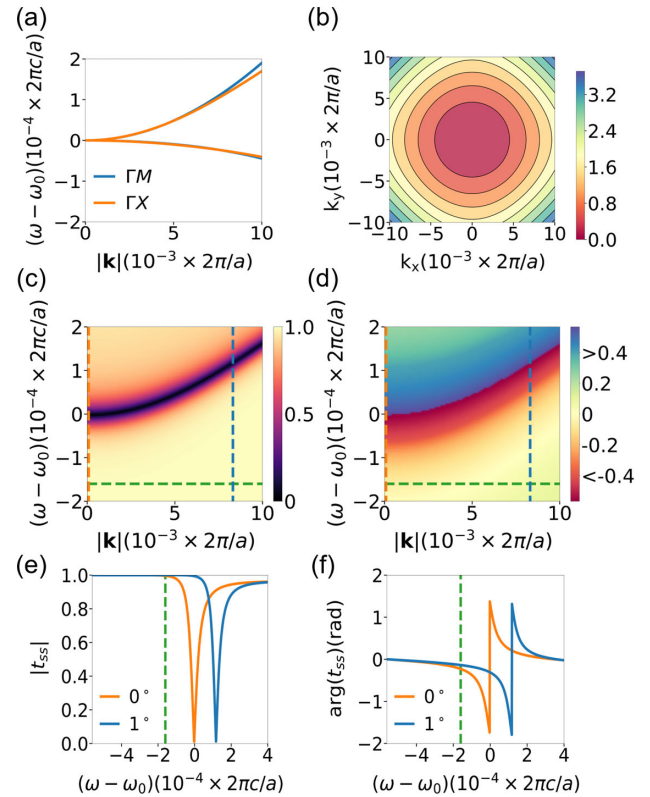


Fig. 2. Band structure and the transmission properties of the photonic crystal slab device shown in Fig. 1(c). (a) Band structure of guided resonances that couples to near-normal incident light, shown along ΓX and ΓM directions. (b) Isofrequency contours of the upper band. (c) Transmission magnitude $|t_{ss}|$ of the incident s -polarized light at different frequencies and in-plane wavevectors. (d) Transmission phase $\arg(t_{ss})$ of the incident s -polarized light at different frequencies and in-plane wavevectors. (e) $|t_{ss}|$ as a function of frequency for s -polarized light with incident angles of 0° and 1° . (f) $\arg(t_{ss})$ as a function of frequency for s -polarized light with incident angles of 0° and 1° . In (c)–(f), the orange and blue lines correspond to the 0° and 1° incidence, respectively, and the green line indicates the operating frequency $\omega_{\text{op}} = 0.47640 \times 2\pi c/a$.

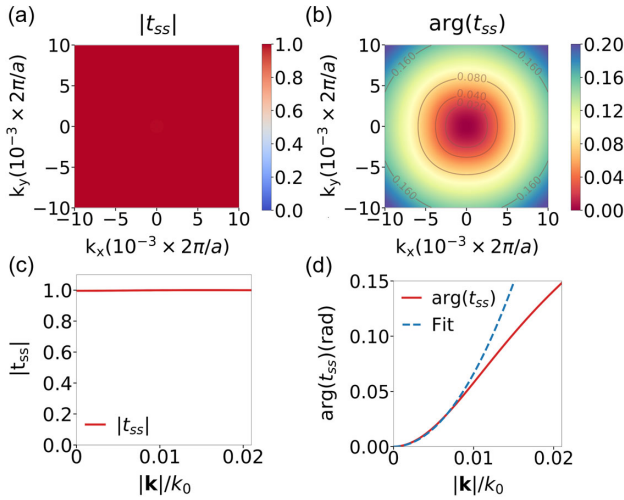


Fig. 3. Transfer function of the photonic crystal slab device. (a) $|t_{ss}|$ as a function of in-plane wavevectors (k_x, k_y) . (b) $\arg(t_{ss})$ as a function of in-plane wavevectors (k_x, k_y) . (c) $|t_{ss}|$ as a function of in-plane wavevector magnitude $|\mathbf{k}|$. $k_0 = \omega_{op}/c$ is the wavenumber at the operating frequency ω_{op} . (d) $\arg(t_{ss})$ as a function of in-plane wavevector magnitude $|\mathbf{k}|$, along with a fit to a quadratic function.

As was noted in Ref. [10], the isotropic band structure leads to the remarkable effect of single-band excitation: *s/p*-polarized light only couples to the upper/lower band, respectively, for every direction of incidence [10]. Consequently, the *s* or *p* polarization is preserved upon transmission through the device ($t_{ps}(\omega, \mathbf{k}) = 0$). We calculate the transmittance of *s*-polarized light $t_{ss}(\omega, \mathbf{k})$ by the Fourier modal method using a freely available software package [28]. Figures 2(c) and 2(d) depict the magnitude $|t_{ss}|$ and phase $\arg(t_{ss})$, respectively, at a general azimuthal angle $\phi = \arctan(k_y/k_x) = 14^\circ$. Due to the isotropic band structure, the results are essentially the same for any other ϕ . The plots clearly show that *s*-polarized light only excites the upper band. The transmission exhibits a sharp dip in magnitude and rapid variation in phase near the band dispersion of the guided resonances.

Figures 2(e) and 2(f) plot the spectra of the transmission magnitude and phase at incident angles $\theta = 0^\circ$ and $\theta = 1^\circ$, respectively. For both incident angles, both the amplitude and phase follows the Fano lineshape formula, as described by Eqs. (12) and (13). As θ increases, the resonance shifts to higher frequencies, consistent with the band structure. Based on Figs. 2(e) and 2(f), we choose the operating frequency at $\omega_{op} = 0.47640 \times 2\pi c/a$ as indicated by the green dashed line. At this frequency, the transmission coefficient magnitude stays close to unity, while the phase varies substantially for varying incident angles, as is required for Eq. (19). Also, we note that at this frequency the corresponding wavelength is greater than the lattice constant such that there is no diffraction due to the slab.

At the operating frequency ω_{op} , Figs. 3(a) and 3(b) show the magnitude and phase of the transmission $t_{ss}(k_x, k_y)$ in the k_x and k_y plane. Figures 3(c) and 3(d) show the magnitude and phase of the transmission along the ΓX direction. The transmission has a magnitude of unity over the entire wavevector range considered [Fig. 3(a)]. Hence, the structure behaves as an all-pass filter in this wavevector range. The phase is isotropic and shows a quadratic dependency of $|\mathbf{k}|$. The magnitude and phase response therefore agrees with Eq. (19).

By fitting the phase response with a quadratic function in $|\mathbf{k}|$, as shown in Fig. 3(d), we obtain the parameter

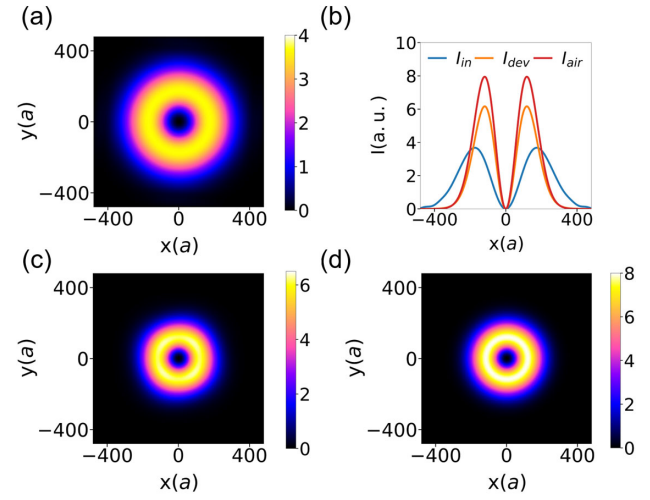


Fig. 4. Demonstration of the device with beam propagation. (a) The intensity distribution of an input converging azimuthally polarized cylindrical vector beam. (b) The radial intensity profile of the three beams in (a), (c), and (d). (c) The intensity distribution of the input beam immediately after passing through 40 devices with a total thickness of $103a$. (d) The intensity distribution of the input beam after a free space propagation of $14823a$.

$\alpha/[\gamma_0(1 + \Omega_0^2)] = 61.97a^2$ for Eq. (19), thus the device is equivalent to free space of a thickness $d_{eff} = 371a$ as determined from Eq. (20). Since the device has a thickness of $d_T = 2.57a$, by replacing the free space with this device, we have preserved the angle-dependent phase response of the free space while reducing the required physical thickness by a compression ratio of $d_{eff}/d_T = 144$. Moreover, since the device behaves as an all-pass filter, a longer effective propagation distance can be achieved by simply cascading multiple devices together. A cascade of N devices results in an effective propagating distance of Nd_{eff} , whereas the compression ratio is unchanged from a single device.

In Fig. 4, we provide a numerical demonstration of the performance of our device [29]. We consider a converging azimuthally (*s*) polarized cylindrical vector beam [30] at the operating frequency ω_{op} . Its intensity distribution at the $z = 0$ plane is shown in Fig. 4(a). For demonstration, we directly simulate a cascade of $N = 40$ devices with an air gap of thickness $0.5a$ between every two neighboring devices. The total thickness of the 40 cascaded devices including the air gaps is $123a$. We numerically calculate the intensity distribution of the transmitted beam after the cascaded devices, as shown in Fig. 4(c). The beam size significantly reduces after passing through the devices. We also numerically verify that the result for 40 devices is indeed the same as that for a single device repeated 40 times. As comparison, in Fig. 4(d), we plot the intensity distribution of the original beam after the propagation in free space by $40d_{eff} = 14823a$. Figures 4(c) and 4(d) agree very well. In Fig. 4(b), we plot the radial profile for the input beam and the aforementioned two output beams. We see that our device can substitute free space propagation and reproduce the beam width and beam shape very well. The reduced peak intensity is caused by the deviation of the transfer function at large wavevectors [Fig. 3(d)].

Our first device above has $NA \approx 0.01$. It can be used to miniaturize low-NA optical systems. Such low-NA systems can provide unique functionalities that cannot be achieved by high-NA systems, but they are usually bulky. One example is telecentric lenses,

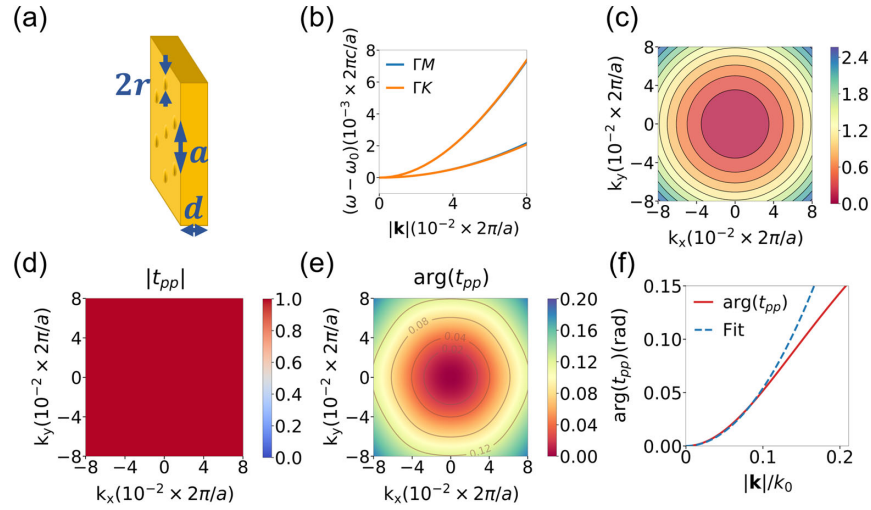


Fig. 5. Another design with a higher NA. (a) The structure is a single-layer photonic crystal slab containing a hexagonal lattice of air holes. The geometric parameters are $r = 0.15a$ and $d = 0.33a$, where a is the lattice constant. The yellow regions correspond to material with permittivity of $\varepsilon = 12$. (b) Band structure of guided resonances that couples to near-normal incident light, shown along the ΓM and ΓK directions. (c) Isofrequency contours of the lower band. (d)–(f) Transfer function of the photonic crystal slab device at the operating frequency $\omega_{\text{op}} = 0.471 \times 2\pi c/a$. (d) $|t_{pp}|$ as a function of wavevectors (k_x, k_y) . (e) $\arg(t_{pp})$ as a function of in-plane wavevectors (k_x, k_y) . (f) $\arg(t_{pp})$ as a function of in-plane wavevector magnitude $|k|$ along with a fit to the quadratic function.

which feature a constant field of view and have important applications in machine vision. They typically exhibit small NA ≈ 0.01 comparable to our device. Our device can significantly reduce the size of these bulky low-NA systems.

Our method can be readily extended to higher-NA systems by choosing suitable design parameters. As a demonstration, we provide another design with a higher NA. Different from the previous one, this device is a single-layer hexagonal photonic crystal slab, as shown in Fig. 5. The slab is also made of materials with a permittivity $\varepsilon = 12$. It has a thickness of $d = 0.33a$ and contains a hexagonal array of circular holes with radius $r = 0.15a$, where a is the lattice constant. Such a slab hosts a pair of guided resonances that are doubly degenerate at the Γ point with the frequency $\omega_0 = 0.47556 \times 2\pi c/a$. Interestingly, for such a photonic crystal slab with the C_{6v} symmetry, it can be proved that the band structure is isotropic near the Γ point. (See Supplement 1 for a proof.) We show the corresponding band structure in Figs. 5(b) and 5(c). Figure 5(b) shows that for each band the dispersion along the ΓK direction coincides with that along the ΓM direction. Figure 5(c) shows that the isofrequency contours for the lower band are almost circular. Again, the isotropic band structure leads to the effect of single-band excitation: s/p -polarized light only couples to the upper/lower band, respectively, for every direction of incidence. (See Supplement 1 for details). As the isotropic band structure is guaranteed by C_{6v} symmetry, we choose suitable geometry parameters d and r to realize the required quality factor Q and background transmission t_d . We consider the light of P polarization at the operating frequency $\omega_{\text{op}} = 0.471 \times 2\pi c/a$. Figures 5(d) and 5(e) show the magnitude and phase of the transmission $t_{pp}(k_x, k_y)$ in the k_x and k_y plane. Figure 5(f) shows the phase of the transmission along the ΓK direction. The transmission has a magnitude of unity over the entire wavevector range considered. The phase is isotropic and exhibits a quadratic dependency of $|k|$. From the fitting, we obtain the equivalent thickness $d_{\text{eff}} = 3.70a$ and a compression ratio $d_{\text{eff}}/d = 11.2$. The working wavevector range of this device is around 10 times larger than the previous

one (cf. Fig. 3), which leads to a much larger NA ≈ 0.11 . (See Supplement 1 for a demonstration of the device performance.) The resonance has a lower quality factor Q than the previous design. Low- Q resonances can be preferable for applications that require a larger spectral bandwidth.

4. DISCUSSION AND CONCLUSION

We note that our device, like free space, is invariant under both translations along the longitudinal direction (i.e., the propagation direction or z direction in Fig. 1) and transverse (i.e., within the $x - y$ plane) directions. Therefore, the device can be inserted anywhere along the optical path, and the effect is independent of the location of insertion. Our device works for both spatially coherent and incoherent optical waves. We also note that our device can work at different frequencies as well, though the equivalent propagation distance can be different. Correction of such a chromatic aberration is of interest for future research.

In the results of the paper above, for illustration purposes, we have only presented results for s - or p -polarized incident beams. Our device can also operate with beams with left/right circular polarizations. When operating with either s or p polarizations, the incident beam corresponds to a cylindrical vector beam. When operating with the circular polarizations, the incident beam needs not be restricted to a cylindrical vector beam but can be other types including Laguerre–Gaussian beams. In our example, the s and p polarizations have different compression ratios. The compression ratios for the left and right circular polarizations are the same and are between those of the s and p polarizations. The difference in the compression ratio between the s and p polarizations is caused by the different dispersions of the two bands. It is possible to achieve polarization-independent compression if one further designs the structure to enforce the two bands having the same effective mass, which will be explored in the future. (See Supplement 1 for a detailed discussion on the polarization response.)

In conclusion, we have shown that free space can be substituted with nonlocal flat optics. We derive the general criteria for replacing free space with an optical device and provide two concrete designs of photonic crystal slab devices. Such a device can substitute much thicker free space. Our work provides an important complement to local flat optics and may prove important for miniaturization of optical systems.

Funding. Air Force Office of Scientific Research (FA9550-17-1-0002); U.S. Department of Defense (N00014-17-1-3030).

Acknowledgment. We acknowledge Dr. Meng Xiao for helpful discussions. This work is supported by the U. S. Air Force Office of Scientific Research (AFOSR) MURI and by the Vannevar Bush Faculty Fellowship from the U. S. Department of Defense. While we were finalizing this paper, a similar recent preprint was brought to our attention (Ref. [31]). Our design here may result in a more compact design as compared with the multilayer configuration shown in Ref. [31].

Disclosures. The authors declare no conflicts of interest.

See [Supplement 1](#) for supporting content.

REFERENCES

1. N. Yu and F. Capasso, "Flat optics with designer metasurfaces," *Nat. Mater.* **13**, 139–150 (2014).
2. A. Arbabi, Y. Horie, M. Bagheri, and A. Faraon, "Dielectric metasurfaces for complete control of phase and polarization with subwavelength spatial resolution and high transmission," *Nat. Nanotechnol.* **10**, 937–943 (2015).
3. M. Khorasaninejad, W. T. Chen, R. C. Devlin, J. Oh, A. Y. Zhu, and F. Capasso, "Metalenses at visible wavelengths: diffraction-limited focusing and subwavelength resolution imaging," *Science* **352**, 1190–1194 (2016).
4. H.-T. Chen, A. J. Taylor, and N. Yu, "A review of metasurfaces: physics and applications," *Rep. Prog. Phys.* **79**, 076401 (2016).
5. P. Genevet, F. Capasso, F. Aieta, M. Khorasaninejad, and R. Devlin, "Recent advances in planar optics: from plasmonic to dielectric metasurfaces," *Optica* **4**, 139–152 (2017).
6. A. Silva, F. Monticone, G. Castaldi, V. Galdi, A. Alu, and N. Engheta, "Performing mathematical operations with metamaterials," *Science* **343**, 160–163 (2014).
7. A. Pors, M. G. Nielsen, and S. I. Bozhevolnyi, "Analog computing using reflective plasmonic metasurfaces," *Nano Lett.* **15**, 791–797 (2015).
8. A. Youssefi, F. Zangeneh-Nejad, S. Abdollahramezani, and A. Khavasi, "Analog computing by Brewster effect," *Opt. Lett.* **41**, 3467–3470 (2016).
9. T. Zhu, Y. Zhou, Y. Lou, H. Ye, M. Qiu, Z. Ruan, and S. Fan, "Plasmonic computing of spatial differentiation," *Nat. Commun.* **8**, 1 (2017).
10. C. Guo, M. Xiao, M. Minkov, Y. Shi, and S. Fan, "Photonic crystal slab Laplace operator for image differentiation," *Optica* **5**, 251–256 (2018).
11. C. Guo, M. Xiao, M. Minkov, Y. Shi, and S. Fan, "Isotropic wavevector domain image filters by a photonic crystal slab device," *J. Opt. Soc. Am. A* **35**, 1685–1691 (2018).
12. T. Zhu, Y. Lou, Y. Zhou, J. Zhang, J. Huang, Y. Li, H. Luo, S. Wen, S. Zhu, Q. Gong, M. Qiu, and Z. Ruan, "Generalized spatial differentiation from the spin hall effect of light and its application in image processing of edge detection," *Phys. Rev. Appl.* **11**, 034043 (2019).
13. T. Davis, F. Eftekhari, D. Gómez, and A. Roberts, "Metasurfaces with asymmetric optical transfer functions for optical signal processing," *Phys. Rev. Lett.* **123**, 013901 (2019).
14. J. Zhou, H. Qian, C.-F. Chen, J. Zhao, G. Li, Q. Wu, H. Luo, S. Wen, and Z. Liu, "Optical edge detection based on high-efficiency dielectric metasurface," *Proc. Natl. Acad. Sci. USA* **116**, 11137–11140 (2019).
15. H. Wang, C. Guo, Z. Zhao, and S. Fan, "Compact incoherent image differentiation with nanophotonic structures," *ACS Photon.* **7**, 338–343 (2020).
16. T. Zhu, J. Huang, and Z. Ruan, "Optical phase mining by adjustable spatial differentiator," *Adv. Photon.* **2**, 016001 (2020).
17. B. E. A. Saleh and M. C. Teich, *Fundamentals of Photonics*, 2nd ed. (Wiley, 2007).
18. J. W. Goodman, *Introduction to Fourier Optics*, 3rd ed. (Roberts & Co, 2005).
19. H. Kwon, D. Sounas, A. Cordaro, A. Polman, and A. Alù, "Nonlocal metasurfaces for optical signal processing," *Phys. Rev. Lett.* **121**, 173004 (2018).
20. W. Zhou, D. Zhao, Y.-C. Shuai, H. Yang, S. Chuwongin, A. Chadha, J.-H. Seo, K. X. Wang, V. Liu, Z. Ma, and S. Fan, "Progress in 2D photonic crystal Fano resonance photonics," *Prog. Quantum Electron.* **38**, 1–74 (2014).
21. M. F. Limonov, M. V. Rybin, A. N. Poddubny, and Y. S. Kivshar, "Fano resonances in photonics," *Nat. Photonics* **11**, 543–554 (2017).
22. W. Zhou and S. Fan, eds., *Photonic Crystal Metasurface Optoelectronics* (Academic, 2019).
23. S. Fan and J. D. Joannopoulos, "Analysis of guided resonances in photonic crystal slabs," *Phys. Rev. B* **65**, 235112 (2002).
24. Z. Zhao, C. Guo, and S. Fan, "Connection of temporal coupled-mode-theory formalisms for a resonant optical system and its time-reversal conjugate," *Phys. Rev. A* **99**, 033839 (2019).
25. A. E. Miroshnichenko, S. Flach, and Y. S. Kivshar, "Fano resonances in nanoscale structures," *Rev. Mod. Phys.* **82**, 2257–2298 (2010).
26. L. C. Andreani and D. Gerace, "Photonic-crystal slabs with a triangular lattice of triangular holes investigated using a guided-mode expansion method," *Phys. Rev. B* **73**, 235114 (2006).
27. M. Minkov and V. Savona, "Automated optimization of photonic crystal slab cavities," *Sci. Rep.* **4**, 5124 (2014).
28. V. Liu and S. Fan, "S4: a free electromagnetic solver for layered periodic structures," *Comput. Phys. Commun.* **183**, 2233–2244 (2012).
29. J. S. Schmidt, *Numerical Simulation of Optical Wave Propagation* (SPIE, 2014).
30. Q. Zhan, "Cylindrical vector beams: from mathematical concepts to applications," *Adv. Opt. Photon.* **1**, 1–57 (2009).
31. O. Reshef, M. P. DelMastro, K. K. M. Bearne, A. H. Alhulaymi, L. Giner, R. W. Boyd, and J. S. Lundeen, "Towards ultra-thin imaging systems: an optic that replaces space," arXiv:2002.06791 (2020).